Lattice Light Shift Evaluations in a Dual-Ensemble Yb Optical Lattice Clock

Tobias Bothwell,[1,*] Benjamin D. Hunt,[1,2,*] Jacob L. Siegel,[1,2,*] Youssef S. Hassan,[1,2] Tanner Grogan,[1,2] Takumi Kobayashi,[1,4] Kurt Gibble,[1,5] Sergey G. Porsev,[6] Marianna S. Safronova,[6] Roger C. Brown,[1] Kyle Beloy,[1] and Andrew D. Ludlow[1,2,3,†]

[1]National Institute of Standards and Technology, 325 Broadway, Boulder, Colorado 80305, USA
[2]University of Colorado, Department of Physics, Boulder, Colorado 80309, USA
[3]Electrical, Computer and Energy Engineering, University of Colorado, Boulder, Colorado 80309, USA
[4]National Metrology Institute of Japan (NMIJ), National Institute of Advanced Industrial Science and Technology (AIST), 1-1-1 Umezono, Tsukuba, Ibaraki 305-8563, Japan
[5]Department of Physics, The Pennsylvania State University, University Park, Pennsylvania 16802, USA
[6]Department of Physics and Astronomy, University of Delaware, Newark, Delaware 19716, USA

(Received 30 August 2024; revised 15 November 2024; accepted 22 November 2024; published 22 January 2025)

In state-of-the-art optical lattice clocks, beyond-electric-dipole polarizability terms lead to a breakdown of magic wavelength trapping. In this Letter, we report a novel approach to evaluate lattice light shifts, specifically addressing recent discrepancies in the atomic multipolarizability term between experimental techniques and theoretical calculations. We combine imaging and multi-ensemble techniques to evaluate lattice light shift atomic coefficients, leveraging comparisons in a dual-ensemble lattice clock to rapidly evaluate differential frequency shifts. Further, we demonstrate application of a running wave field to probe both the multipolarizability and hyperpolarizability coefficients, establishing a new technique for future lattice light shift evaluations.

DOI: 10.1103/PhysRevLett.134.033201

Optical lattice clocks (OLCs) are among the most accurate [1–4] and precise [5–8] sensors ever created by humankind, positioning them as strong candidates for the redefinition of the SI second [9]. Modern clock performance further supports studies of fundamental physics, from searches for dark matter [10,11] to tests of general relativity [12,13]. In parallel, emerging transportable OLCs promise to revolutionize relativistic geodesy, mapping Earth's geoid to new levels [14].

Central to OLC performance is the trapping of ultracold atoms at the so-called magic wavelength (or frequency) [15,16], where the differential dynamic polarizability between clock electronic states vanishes. The resulting differential light shift is fundamental to OLCs and is an accuracy-limiting systematic effect [2,4]. Higher-order perturbations from magic wavelength trapping, such as magnetic-dipole and electric-quadrupole terms (so-called multipolarizability) [17], produce nontrival couplings between the resulting light shifts and the motional states of the atomic sample, challenging the efficacy of magic wavelength trapping. Careful characterization of these shifts is ongoing. Multiple experimental evaluations of these higher-multipolar corrections in ^{87}Sr [18–20], combined with recent theoretical development [21,22], have resolved disagreement of both the sign and magnitude of the multipolarizabilty coefficient. In ^{171}Yb, disagreement remains between a single experimental result [23] and theoretical calculations [24–26].

Simultaneously, recent efforts have demonstrated how imaging techniques combined with multi-ensemble operation may be used to enhance the measurement capabilities of OLCs [27]. For example, differential measurements made by synchronous comparison between multiple optical clocks [5,6] or within a single clock system [7] reject common mode laser noise, realizing an effective decoherence-free subspace [27,28]. Such techniques in 1D OLCs have demonstrated remarkable progress, observing the gravitational redshift at the millimeter scale [13] and utilizing multi-apparatus operation for extended coherence times [5,29].

In this Letter we demonstrate application of emerging multi-ensemble techniques to a full differential polarizability evaluation in an Yb OLC. Our experimental apparatus, described in previous publications [2,30], is a standard OLC utilizing a vertical retro-reflected 1D magic wavelength optical lattice at 759 nm. Here, we employ a recently demonstrated "ratchet loading" technique [31]. We load two spatially separated ensembles using a combination of magnetic field control during MOT operation and shelving to the metastable clock state (see Fig. 1). We then employ clock-mediated Sisyphus cooling [30] to achieve radial temperatures of ~600 nK and sideband

*These authors contributed equally to this work.
†Contact author: andrew.ludlow@nist.gov

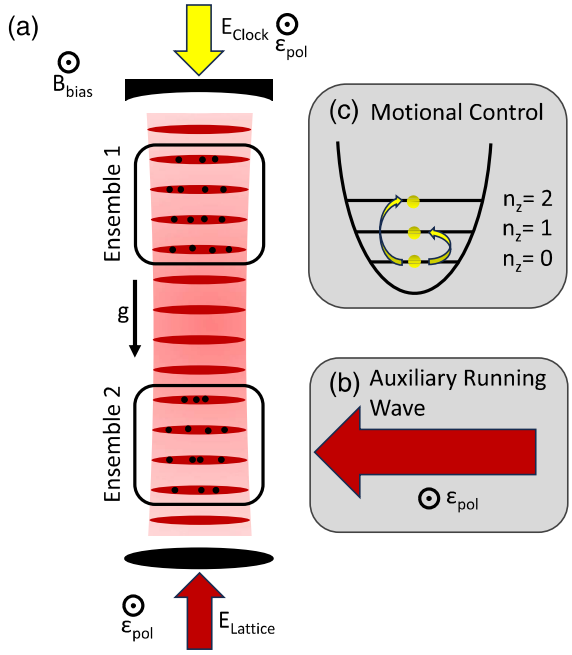

FIG. 1. (a) Schematic of a dual-ensemble 1D Yb OLC (not to scale). The 759 nm lattice is formed via retroreflection of a single beam and clock light is introduced through the mirror used for reflection of the 759 nm beam. The directions of the polarization, magnetic field, and gravity orientation are indicated. (b) A 759 nm transverse running wave may be introduced to ensemble 2, allowing evaluation of the running wave magic wavelength and hyperpolarizability via differential comparisons. (c) The longitudinal motional state of the atoms in each ensemble may be manipulated separately, providing enhanced, differential sensitivity to higher-order light shift terms.

cooling to prepare atoms in the ground longitudinal band, providing a more uniform sampling of the lattice antinodes. This dual-ensemble preparation forms the basis of the experiments reported in this Letter, allowing differential measurements between the ensembles. Details of the dual-ensemble preparation are given in the Supplemental Material [32].

Near the magic wavelength, the lattice light shift $\delta\nu_{LS}$ can be written as a function of trap depth U, detuning δ_L of lattice frequency ν_L from the electric dipole ($E1$) magic frequency ν_{E1} ($\delta_L = \nu_L - \nu_{E1}$), radial temperature T_r, and longitudinal vibrational state n_z. For simplicity we follow Ref. [18], adopting a light shift model utilizing a harmonic basis (see Appendix A for a complementary treatment with a more general model). The lattice light shift is then given by

$$\frac{\delta\nu_{LS}(u,\delta_L,n_z)}{\nu_c} \approx \left(\frac{\partial\tilde{\alpha}_{E1}}{\partial\nu}\delta_L - \tilde{\alpha}_{M1E2}\right)(n_z+1/2)u^{1/2} - \left[\frac{\partial\tilde{\alpha}_{E1}}{\partial\nu}\delta_L + \frac{3}{2}\tilde{\beta}\left(n_z^2+n_z+\frac{1}{2}\right)\right]u + 2\tilde{\beta}\left(n_z+\frac{1}{2}\right)u^{3/2} - \tilde{\beta}u^2, \quad (1)$$

where we have divided the clock shift ($\delta\nu_{LS}$) by the clock frequency (ν_c) and utilize normalized trap depths $u = U/E_R$. $E_R = (h\nu_L)^2/2mc^2$ is the recoil energy and c the speed of light, m the atomic mass, and h Planck's constant. The effects of transverse temperatures are captured via an effective depth $u^j \to (1 + jk_BT_r/uE_R)^{-1}u^j$ [18,52], where j is the power series exponent for each term in Eq. (1). k_B is the Boltzmann constant and trap depth is measured via sideband spectroscopy [53]. All trap depths u^j in the Letter implicitly assume this effective radial thermal averaging.

Complete lattice light shift evaluations require knowledge of ν_{E1} and the three differential atomic coefficients within Eq. (1). $(\partial\tilde{\alpha}_{E1}/\partial\nu)$ is the linear slope of the differential $E1$ polarizability between the ground ($^1S_0$) and excited ($^3P_0$) clock states arising from a Taylor expansion about ν_{E1}. $\tilde{\alpha}_{M1E2}$ and $\tilde{\beta}$ are the differential multipolarizability and hyperpolarizability, respectively. These coefficients are often evaluated via interleaved comparisons between two trap depths (u) [26] or two motional states (n_z) [18]. By operating over a broad range of trap depths, lattice frequencies, and motional states, individual polarizability terms can be disentangled and measured. In many OLCs, however, practical limits of the realizable trap depths make such an evaluation daunting at the state-of-the-art level. Here, we overcome this limitation by supplementing the standard evaluation techniques with imaging and multi-ensemble operation.

Evaluation of $\partial\tilde{\alpha}_{E1}/\partial\nu$—The only terms in Eq. (1) that include $(\partial\tilde{\alpha}_{E1}/\partial\nu)$ are proportional to δ_L (and vice versa). Therefore, single ensemble measurements of the light shift taken by temporally self-interleaving between two lattice detunings δ_1 and δ_2 allow $(\partial\tilde{\alpha}_{E1}/\partial\nu)$ to be isolated. With the same preparation conditions, the frequency difference is

$$\frac{\Delta\nu_\delta(u,\delta_1,\delta_2,n_z)}{\nu_c} = -\frac{\partial\tilde{\alpha}_{E1}}{\partial\nu}(\delta_2-\delta_1)u', \quad (2)$$

where we have introduced $u' = [u - (n_z + 1/2)u^{1/2}]$. Critically, such self-interleaved measurements are independent of $\tilde{\alpha}_{M1E2}$, $\tilde{\beta}$, and ν_{E1}, while also differentially rejecting cold collision shifts. As shown in Fig. 2, we perform these measurements at four trap depths with $\delta_2 - \delta_1 = -108.2(2)$ MHz and find $(\partial\tilde{\alpha}_{E1}/\partial\nu) = 4.2(1) \times 10^{-20}$/MHz, in excellent agreement with previous measurements [2,54].

Evaluation of $\tilde{\beta}$—We now turn to the remaining atomic coefficients in Eq. (1). At the limited trap depths available in our apparatus ($< 140\ E_R$), evaluation of these shifts with standard interleaved measurements is challenging. Instead, we utilize imaging and dual-ensemble operation as shown in Fig. 1. Frequency comparisons between the two ensembles (found by converting differences in excitation probabilities to frequency via the known Rabi line shape [32]) are insensitive to laser frequency-noise, providing enhanced relative stability [8,27]. We regularly measure frequency instabilities of $\sim 4 \times 10^{-17}$ at 1 s for

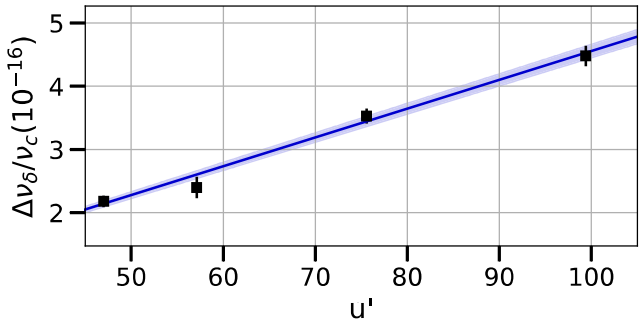

FIG. 2. $(\partial\tilde{\alpha}_{E1}/\partial\nu)$ is measured by temporally self-interleaving between lattice frequency detunings δ_2 and δ_1 for a single ensemble. The frequency shift, with error bars derived from the Allan deviation at half the total measurement time, is plotted versus u'. A zero-intercept linear fit, with 1σ error bars (shaded region), gives $(\partial\tilde{\alpha}_{E1}/\partial\nu)$ as the slope.

synchronous comparison between ensembles as compared with $\sim 3\times10^{-16}$ for temporally self-interleaved measurements, allowing us to evaluate shifts nearly 50 times faster.

We apply an auxiliary running wave field to the second ensemble [Fig. 1(b)], near the magic frequency (but $>$ MHz detuned from the standing wave laser frequency). For a running wave the $E1$ polarizability and multipolarizability terms simply add, in contrast to a standing wave where they are out of phase. The fractional frequency shift from the addition of an auxiliary running wave to the standing wave is

$$\frac{\delta\nu_R(u_r,u',\delta_r)}{\nu_c}\approx-\left(\frac{\partial\tilde{\alpha}_{E1}}{\partial\nu}\delta_r+\tilde{\alpha}_{M1E2}+\tilde{\beta}_d u'\right)u_r, \quad (3)$$

where u_r is the running wave "depth," u' the average standing wave depth experienced by the atoms [as introduced in Eq. (2)], $\delta_r=\nu_r-\nu_{E1}$, and ν_r the running wave frequency (note that shifts of order u_r^2 and higher have been omitted here [32]). Equation (3) includes a shift term that is $\propto u'u_r$, arising from the dichromatic hyperpolarizability $\tilde{\beta}_d$ [55,56]. For parallel linear lattice and running wave polarizations (Fig. 1), the dichromatic hyperpolarzability is related to the more familiar hyperpolarzability of Eq. (1) by $\tilde{\beta}_d=4\tilde{\beta}$ [56]. This interference effect provides a new method to determine $\tilde{\beta}$ with minimal correlation to ν_{E1} [26]. Further, the use of synchronous dual-ensemble measurements facilitates its precise determination at shallow lattice depths. The auxiliary field has a u'-dependent frequency $\nu_r'(u')$ where $\delta\nu_R(u_r,u',\nu_r'-\nu_{E1})=0$, given by

$$\nu_r'(u')=\left(\nu_{E1}-\frac{\tilde{\alpha}_{M1E2}}{\frac{\partial\tilde{\alpha}_{E1}}{\partial\nu}}\right)-\frac{4\tilde{\beta}u'}{\frac{\partial\tilde{\alpha}_{E1}}{\partial\nu}}. \quad (4)$$

$\nu_r'(u')$ is a linear function of u' with a slope revealing $\tilde{\beta}$ and an offset $\nu_r'(0)=\nu_{E1}-\tilde{\alpha}_{M1E2}/(\partial\tilde{\alpha}_{E1}/\partial\nu)$, directly relating ν_{E1} and $\tilde{\alpha}_{M1E2}$.

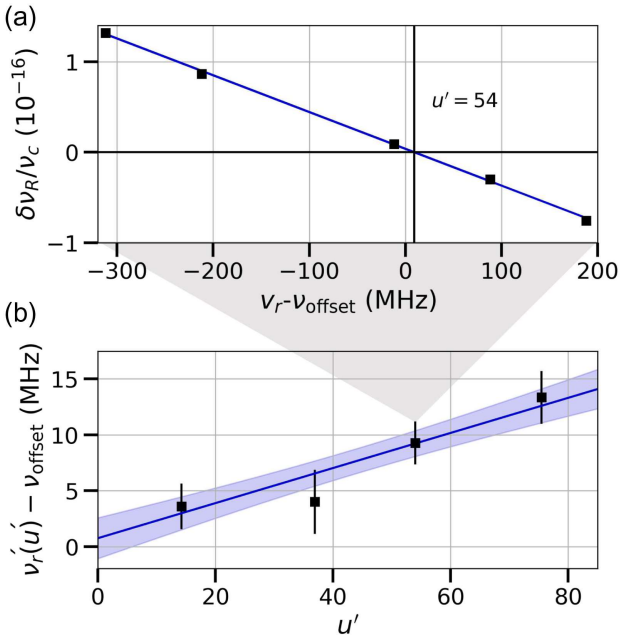

FIG. 3. Measurement of the running wave magic frequency, $\nu_r'(u')$. (a) The frequency shift arising from the addition of a running wave, measured synchronously, is plotted versus the running wave frequency, ν_r. Error bars are smaller than the point size and $\nu_{\rm offset}=394\,798\,300$ MHz. We show the fit for a $u'=54$ standing wave contribution with black lines showing the fitted intercept for $\nu_r'(u')$. (b) $\nu_r'(u')$ is plotted versus u' for each of the four evaluated depths. The blue line and associated 1σ statistical uncertainty region show the fit to Eq. (4).

To experimentally evaluate $\nu_r'(u')$ we apply a running wave beam with a waist of $\approx$150 μm to ensemble 2. We evaluate the ensemble-averaged depth to be $u_r\approx10$, calibrated *in situ* by dividing the slope of Fig. 3(a) by $-(\partial\tilde{\alpha}_{E1}/\partial\nu)$. In this experiment, we do not apply Sisyphus cooling to lower the radial temperature, unlike all other measurements in this Letter, as the addition of the running wave interferes with the optical access used for cooling. At four different standing wave depths the running wave frequency is stepped over 500 MHz centered around the approximate location of $\nu_r'(u')$ (see Fig. 3). From these measurements a linear fit gives $\tilde{\beta}=-1.7(4)\times10^{-21}$ and $\nu_r'(0)=394\,798\,300.4(18)$ MHz. This value of $\tilde{\beta}$ falls between previous measurements using relatively deep optical lattices [23,26] and is in good agreement with independent evaluations made via two-photon resonances [57,58].

Evaluation of $\tilde{\alpha}_{M1E2}$ and ν_{E1}—Returning to Fig. 1, we may prepare ensemble 1 in $n_z\approx0$ and ensemble 2 in either $n_z\approx1$ or $n_z\approx2$ [32]. This allows differential comparisons between ensembles to be preferentially sensitive to the $\tilde{\alpha}_{M1E2}$ dominated $\sqrt{u}$ term of Eq. (1). The differential lattice light shift between samples with motional states n_1 and n_2 is given by

$$\frac{\Delta\nu_{n_z}(u,\delta_r',n_1,n_2)}{\nu_c} \approx \left(\frac{\partial\tilde{\alpha}_{E1}}{\partial\nu}\delta_r' - 2\tilde{\alpha}_{M1E2}\right)(n_2-n_1)u^{1/2} - \frac{3}{2}\tilde{\beta}(n_2^2+n_2-n_1^2-n_1)u + 2\tilde{\beta}(n_2-n_1)u^{3/2}, \quad (5)$$

with $\delta_r' = [\nu_L - \nu_r'(0)]$. Note the elimination of ν_{E1} in Eq. (5) by substitution of $\nu_r'(0)$ into Eq. (1). With the determinations of $(\partial\tilde{\alpha}_{E1}/\partial\nu)$, $\nu_r'(0)$, and $\tilde{\beta}$ in hand, this leaves only $\tilde{\alpha}_{M1E2}$ to evaluate.

As shown in Fig. 4, we perform differential n_z experiments at a variety of trap depths. The shift is shown normalized by the differential n_z applied between ensembles, highlighting the $\sqrt{u}$ dependence (fit shown in blue). The radial temperatures are measured for each ensemble, and n_z-dependent cold collision corrections are applied [32]. A Monte Carlo method is used to propagate sources of uncertainty from both measured atomic coefficients and model inputs to the fit of each ensemble to Eq. (1). We find $\tilde{\alpha}_{M1E2} = -1.41(9)\times10^{-18}$, in good agreement with a previous measurement at lower precision [23]. Finally, $\tilde{\alpha}_{M1E2}$ is substituted back into the definition of $\nu_r'(0)$, giving $\nu_{E1} = 394\,798\,266.9(26)$ MHz. Table I summarizes our experimental results.

Theoretical predictions of $\tilde{\alpha}_{M1E2}$—It is now recognized that earlier calculations for Yb [24–26], Sr [24,25,55,59,60], and other alkaline-earth(-like) systems

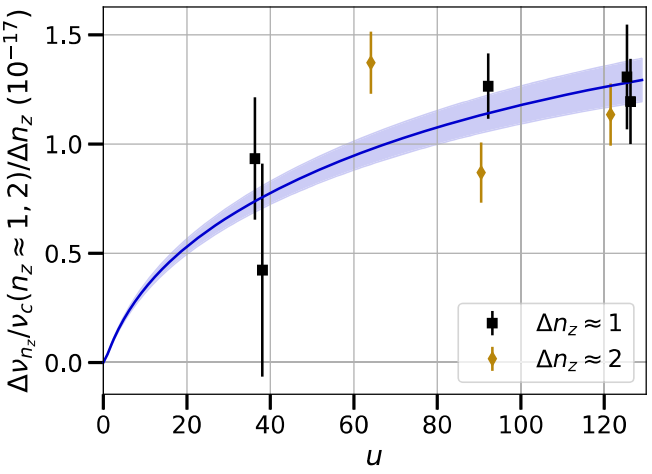

FIG. 4. $\tilde{\alpha}_{M1E2}$ is measured via synchronous comparison of $n_z\approx0$ to $n_z\approx1$ (black squares) and to $n_z\approx2$ (gold diamonds). The fit to $\Delta\nu_{n_z}/\nu_c$, Eq. (5), is shown in blue, with associated 1σ statistical uncertainty shaded. We plot the shifts normalized by $\Delta n_z = n_2 - n_1$ to highlight the $\sqrt{u}$ dependence predominantly arising from $\tilde{\alpha}_{M1E2}$. State-preparation errors resulted in $\Delta n_z \approx 1 \to 0.8$ and $\Delta n_z \approx 2 \to 1.3$ [32]. As a result, the plotted fit to Eq. (5) is meant as a visual guide as it assumes perfect state preparation. A Monte Carlo fit to Eq. (1) for each ensemble is required to fully account for n_z and other experimental values, with the results in Table I. A reduced chi-squared of 1.7 is found.

TABLE I. Summary of experimental and theoretical values derived from this Letter. See Appendix A for a complementary Born-Oppenheimer + WKB treatment [52].

Coefficient	Value
$(\partial\tilde{\alpha}_{E1}/\partial\nu)$ $(10^{-20}/\text{MHz})$	4.2(1)
$\tilde{\beta}$ (10^{-21})	−1.7(4)
$\tilde{\alpha}_{M1E2}^{\text{Experiment}}$ (10^{-18})	−1.41(9)
$\tilde{\alpha}_{M1E2}^{\text{Theory}}$ (10^{-18})	−1.9(5)
ν_{E1} (MHz)	394 798 266.9(26)
$\nu_r'(0)$ (MHz)	394 798 300.4(18)

[24,25,61–64] did not include the important diamagnetic contribution to the $M1$ polarizability at the magic wavelength. This resulted in a disagreement between theoretical and experimental results [18–20,23], recently resolved in the case of Sr [21,22]. The diamagnetic shift has been discussed extensively in the literature for the case of uniform dc magnetic fields (e.g., Refs. [65–67]). In a nonrelativistic treatment, the diamagnetic shift appears at first order in perturbation theory and is proportional to the expectation value $\langle r^2\rangle$, where r denotes the distance from the electron to the nucleus, a sum over all electrons is implied, and a total electronic angular momentum $J = 0$ is assumed. In a relativistic treatment starting from the Dirac equation, the emergence of the diamagnetic shift is less conspicuous. It arises at second order in perturbation theory, being attributed to negative-energy (positron) states in the summation over states. However, it can be reformulated in terms of the expectation value $\langle\beta r^2\rangle$, where β is a conventional 4×4 Dirac matrix [65,66]. Evaluated between Dirac bispinors, the operators r^2 and βr^2 have contributions attributed to large and small components of the Dirac bispinors. The inclusion of β merely effects a sign change for the small-component contribution, which vanishes in the nonrelativistic limit [67].

TABLE II. $M1$ differential polarizability, evaluated in the dc limit and at the magic frequency. Theoretical contributions include the $^3P_0 - {}^3P_1$ paramagnetic (positive energy state) contribution, the diamagnetic (negative energy state) contribution, and other smaller contributions. This is an abbreviated version of a more expansive table presented in the Supplemental Material [32], which also includes discussion of theoretical uncertainties. For the dc limit, the final theoretical value is compared to the experimental value. All values are in 10^{-3} a.u., where a.u. denotes atomic units based on Gaussian electromagnetic expressions.

Contribution	dc limit	Magic frequency
$^3P_0 - {}^3P_1$	5.469	−0.016
Diamagnetic	−0.099	−0.099
Other	0.008	−0.002
Total	5.379(10)	−0.116(5)
Experiment [2,68]	5.363(6)	

For Yb, we start by considering the differential $M1$ polarizability in the dc limit. Table II presents a breakdown of contributions calculated as detailed in the Supplemental Material [32]. The final results are compared to the experimental value, which has a 0.1% uncertainty [2,68]. As expected, we find that the $^3P_0$–$^3P_1$ "paramagnetic" contribution dominates, in part due to a small energy denominator (i.e., the fine structure splitting) in the second-order summation over states. Meanwhile, we find that the diamagnetic contribution amounts to a ∼2% correction, with other contributions being an order of magnitude smaller still. Though subdominant, the diamagnetic contribution is non-negligible in the theory-experiment comparison, exemplifying its role in the differential $M1$ polarizability.

We next consider the differential $M1$ polarizability evaluated at the magic wavelength (see Table II and [32]). We find that, relative to the dc limit, the $^3P_0$–$^3P_1$ paramagnetic contribution is largely suppressed, a consequence of the lattice photon energy being much greater than the fine structure splitting. Meanwhile, the dc value for the diamagnetic contribution can be directly applied for the magic wavelength case, as the photon energy is significantly below the energy associated with electron-positron pair production. It follows that the diamagnetic contribution becomes the dominant contribution for the differential $M1$ polarizability at the magic wavelength. Further, evaluating and including the differential $E2$ polarizability at the magic wavelength [32], we obtain the theoretical result $\tilde{\alpha}_{M1E2} = -1.9(5) \times 10^{-18}$, in good agreement with the experimental results (Table I). Finally, using formalism described in Ref. [59] we found $\tilde{\beta} = -2.3 \times 10^{-21}$ in the CI + all-order approximation. In two dominant terms, we replaced the theoretical denominators with more correct experimental ones, that strongly affect the result. We consider the result an order of magnitude estimate.

Summary—With multi-ensemble operation and imaging, we realize a complete lattice light shift evaluation of a standard retroreflected 1D OLC using modest trap depths. Our independent evaluation provides valuable atomic coefficients for Yb OLCs while also demonstrating novel techniques for the evaluation of both $(\partial\tilde{\alpha}_{E1}/\partial\nu)$, $\tilde{\beta}$, and $\tilde{\alpha}_{M1E2}$ [55]. Finally, the experimental and theoretical results from this Letter further validate the recent consensus on the origin of the disagreement on the sign and magnitude of the multipolarizability term $\tilde{\alpha}_{M1E2}$.

Acknowledgments—We thank K. Kim and A. Staron for careful reading of the manuscript. T. B. acknowledges insightful conversations with A. Goban and R. Hutson. The experimental work was supported by NIST, ONR, and NSF QLCI Grants No. 2016244 and No. 2012117 (K. G.). T. B. acknowledges support from the NRC RAP. The theoretical work has been supported in part by the U.S. NSF Grants No. PHY-2309254, No. OMA-2016244, U.S. Office of Naval Research Grant No. N00014-20-1-2513, and by the European Research Council (ERC) under the Horizon 2020 Research and Innovation Program of the European Union (Grant Agreement No. 856415). Calculations in this work were done through the use of Information Technologies resources at the University of Delaware, specifically the high-performance Caviness and DARWIN computer clusters.

[1] I. Ushijima, M. Takamoto, M. Das, T. Ohkubo, and H. Katori, Cryogenic optical lattice clocks, Nat. Photonics **9**, 185 (2015).
[2] W. McGrew, X. Zhang, R. Fasano, S. Schäffer, K. Beloy, D. Nicolodi, R. Brown, N. Hinkley, G. Milani, M. Schioppo *et al.*, Atomic clock performance enabling geodesy below the centimetre level, Nature (London) **564**, 87 (2018).
[3] T. Bothwell, D. Kedar, E. Oelker, J. M. Robinson, S. L. Bromley, W. L. Tew, J. Ye, and C. J. Kennedy, JILA Sri optical lattice clock with uncertainty of 2×10^{-18}, Metrologia **56**, 065004 (2019).
[4] A. Aeppli, K. Kim, W. Warfield, M. S. Safronova, and J. Ye, Clock with 8×10^{-19} systematic uncertainty, Phys. Rev. Lett. **133**, 023401 (2024).
[5] M. Schioppo, R. C. Brown, W. F. McGrew, N. Hinkley, R. J. Fasano, K. Beloy, T. Yoon, G. Milani, D. Nicolodi, J. Sherman *et al.*, Ultrastable optical clock with two cold-atom ensembles, Nat. Photonics **11**, 48 (2017).
[6] E. Oelker, R. Hutson, C. Kennedy, L. Sonderhouse, T. Bothwell, A. Goban, D. Kedar, C. Sanner, J. Robinson, G. Marti *et al.*, Demonstration of 4.8×10^{-17} stability at 1 s for two independent optical clocks, Nat. Photonics **13**, 714 (2019).
[7] X. Zheng, J. Dolde, V. Lochab, B. N. Merriman, H. Li, and S. Kolkowitz, Differential clock comparisons with a multiplexed optical lattice clock, Nature (London) **602**, 425 (2022).
[8] T. Bothwell, C. J. Kennedy, A. Aeppli, D. Kedar, J. M. Robinson, E. Oelker, A. Staron, and J. Ye, Resolving the gravitational redshift across a millimetre-scale atomic sample, Nature (London) **602**, 420 (2022).
[9] N. Dimarcq, M. Gertsvolf, G. Mileti, S. Bize, C. Oates, E. Peik, D. Calonico, T. Ido, P. Tavella, F. Meynadier *et al.*, Roadmap towards the redefinition of the second, Metrologia **61**, 012001 (2024).
[10] A. Derevianko and M. Pospelov, Hunting for topological dark matter with atomic clocks, Nat. Phys. **10**, 933 (2014).
[11] C. J. Kennedy, E. Oelker, J. M. Robinson, T. Bothwell, D. Kedar, W. R. Milner, G. E. Marti, A. Derevianko, and J. Ye, Precision metrology meets cosmology: Improved constraints on ultralight dark matter from atom-cavity frequency comparisons, Phys. Rev. Lett. **125**, 201302 (2020).
[12] M. Takamoto, I. Ushijima, N. Ohmae, T. Yahagi, K. Kokado, H. Shinkai, and H. Katori, Test of general relativity by a pair of transportable optical lattice clocks, Nat. Photonics **14**, 411 (2020).
[13] X. Zheng, J. Dolde, M. C. Cambria, H. M. Lim, and S. Kolkowitz, A lab-based test of the gravitational redshift with a miniature clock network, Nat. Commun. **14**, 4886 (2023).

[14] T. E. Mehlstäubler, G. Grosche, C. Lisdat, P. O. Schmidt, and H. Denker, Atomic clocks for geodesy, Rep. Prog. Phys. **81**, 064401 (2018).

[15] M. Takamoto and H. Katori, Spectroscopy of the $^1S_0 - {}^3P_0$ clock transition of ^{87}Sr in an optical lattice, Phys. Rev. Lett. **91**, 223001 (2003).

[16] J. Ye, H. Kimble, and H. Katori, Quantum state engineering and precision metrology using state-insensitive light traps, Science **320**, 1734 (2008).

[17] A. V. Taichenachev, V. I. Yudin, V. D. Ovsiannikov, V. G. Pal'Chikov, and C. W. Oates, Frequency shifts in an optical lattice clock due to magnetic-dipole and electric-quadrupole transitions, Phys. Rev. Lett. **101**, 193601 (2008).

[18] I. Ushijima, M. Takamoto, and H. Katori, Operational magic intensity for Sr optical lattice clocks, Phys. Rev. Lett. **121**, 263202 (2018).

[19] S. Dörscher, J. Klose, S. Maratha Palli, and C. Lisdat, Experimental determination of the $E2-M1$ polarizability of the strontium clock transition, Phys. Rev. Res. **5**, L012013 (2023).

[20] K. Kim, A. Aeppli, T. Bothwell, and J. Ye, Evaluation of lattice light shift at low 10^{-19} uncertainty for a shallow lattice Sr optical clock, Phys. Rev. Lett. **130**, 113203 (2023).

[21] F.-F. Wu, T.-Y. Shi, W.-T. Ni, and L.-Y. Tang, Contribution of negative-energy states to the $E2-M1$ polarizability of optical clocks, Phys. Rev. A **108**, L051101 (2023).

[22] S. G. Porsev, M. G. Kozlov, and M. S. Safronova, Contribution of negative-energy states to multipolar polarizabilities of the Sr optical lattice clock, Phys. Rev. A **108**, L051102 (2023).

[23] N. Nemitz, A. A. Jørgensen, R. Yanagimoto, F. Bregolin, and H. Katori, Modeling light shifts in optical lattice clocks, Phys. Rev. A **99**, 033424 (2019).

[24] H. Katori, V. D. Ovsiannikov, S. I. Marmo, and V. G. Palchikov, Strategies for reducing the light shift in atomic clocks, Phys. Rev. A **91**, 052503 (2015).

[25] V. D. Ovsiannikov, S. I. Marmo, V. G. Palchikov, and H. Katori, Higher-order effects on the precision of clocks of neutral atoms in optical lattices, Phys. Rev. A **93**, 043420 (2016).

[26] R. C. Brown, N. B. Phillips, K. Beloy, W. F. McGrew, M. Schioppo, R. J. Fasano, G. Milani, X. Zhang, N. Hinkley, H. Leopardi *et al.*, Hyperpolarizability and operational magic wavelength in an optical lattice clock, Phys. Rev. Lett. **119**, 253001 (2017).

[27] G. E. Marti, R. B. Hutson, A. Goban, S. L. Campbell, N. Poli, and J. Ye, Imaging optical frequencies with 100 μHz precision and 1.1 μm resolution, Phys. Rev. Lett. **120**, 103201 (2018).

[28] T. Manovitz, R. Shaniv, Y. Shapira, R. Ozeri, and N. Akerman, Precision measurement of atomic isotope shifts using a two-isotope entangled state, Phys. Rev. Lett. **123**, 203001 (2019).

[29] M. E. Kim, W. F. McGrew, N. V. Nardelli, E. R. Clements, Y. S. Hassan, X. Zhang, J. L. Valencia, H. Leopardi, D. B. Hume, T. M. Fortier, A. D. Ludlow, and D. R. Leibrandt, Improved interspecies optical clock comparisons through differential spectroscopy, Nat. Phys. **19**, 25 (2023).

[30] C.-C. Chen, J. L. Siegel, B. D. Hunt, T. Grogan, Y. S. Hassan, K. Beloy, K. Gibble, R. C. Brown, and A. D. Ludlow, Clock-line-mediated sisyphus cooling, Phys. Rev. Lett. **133**, 053401 (2024).

[31] Y. S. Hassan, T. Kobayashi, T. Bothwell, J. L. Siegel, B. D. Hunt, K. Beloy, K. Gibble, T. Grogan, and A. Ludlow, Ratchet loading and multi-ensemble operation in an optical lattice clock, Quantum Sci. Technol. **9**, 045023 (2024).

[32] See Supplemental Material at http://link.aps.org/supplemental/10.1103/PhysRevLett.134.033201, which contains Refs. [33–51], for details on dual-ensemble loading, longitudinal state preparation, running wave light shifts, frequency comparisons, comprehensive tables of theoretical contributions to the $M1$ and $E2$ polarizabilities, and description of theoretical uncertainty.

[33] X. Zhang, K. Beloy, Y. S. Hassan, W. F. McGrew, C.-C. Chen, J. L. Siegel, T. Grogan, and A. D. Ludlow, Subrecoil clock-transition laser cooling enabling shallow optical lattice clocks, Phys. Rev. Lett. **129**, 113202 (2022).

[34] D. Leibfried, R. Blatt, C. Monroe, and D. Wineland, Quantum dynamics of single trapped ions, Rev. Mod. Phys. **75**, 281 (2003).

[35] T. L. Nicholson, A new record in atomic clock performance, Ph.D. thesis, University of Colorado Boulder, CO, USA, 2015.

[36] T. L. Nicholson, S. Campbell, R. Hutson, G. E. Marti, B. Bloom, R. L. McNally, W. Zhang, M. Barrett, M. S. Safronova, G. Strouse *et al.*, Systematic evaluation of an atomic clock at 2×10^{-18} total uncertainty, Nat. Commun. **6**, 6896 (2015).

[37] D. A. Steck, Quantum and atom optics (2007), https://atomoptics.uoregon.edu/~dsteck/teaching/quantum-optics/.

[38] A. D. Ludlow, The strontium optical lattice clock: optical spectroscopy with sub-Hertz accuracy, Ph.D. thesis, University of Colorado at Boulder, 2008.

[39] A. D. Ludlow, M. M. Boyd, J. Ye, E. Peik, and P. O. Schmidt, Optical atomic clocks, Rev. Mod. Phys. **87**, 637 (2015).

[40] S. G. Porsev, A. Derevianko, and E. N. Fortson, Possibility of an optical clock using the $6^1S_0 \rightarrow 6^3P_0^o$ transition in ^{171,173}Yb atoms held in an optical lattice, Phys. Rev. A **69**, 021403(R) (2004).

[41] V. A. Dzuba, V. V. Flambaum, and M. G. Kozlov, Combination of the many-body perturbation theory with the configuration-interaction method, Phys. Rev. A **54**, 3948 (1996).

[42] M. S. Safronova, M. G. Kozlov, W. R. Johnson, and D. Jiang, Development of a configuration-interaction plus all-order method for atomic calculations, Phys. Rev. A **80**, 012516 (2009).

[43] R. M. Sternheimer, On nuclear quadrupole moments, Phys. Rev. **80**, 102 (1950).

[44] A. Dalgarno and J. T. Lewis, The exact calculation of long-range forces between atoms by perturbation theory, Proc. R. Soc. A **233**, 70 (1955).

[45] D. M. Jones, F. van Kann, and J. J. McFerran, Intercombination line frequencies in ^{171}Yb validated with the clock transition, Appl. Opt. **62**, 3932 (2023).

[46] S. M. Brewer, J.-S. Chen, K. Beloy, A. M. Hankin, E. R. Clements, C. W. Chou, W. F. McGrew, X. Zhang, R. J. Fasano, D. Nicolodi, H. Leopardi, T. M. Fortier, S. A. Diddams, A. D. Ludlow, D. J. Wineland, D. R. Leibrandt, and D. B. Hume, Measurements of $^{27}Al^+$ and $^{25}Mg^+$ magnetic constants for improved ion-clock accuracy, Phys. Rev. A **100**, 013409 (2019).

[47] M. M. Boyd, T. Zelevinsky, A. D. Ludlow, S. Blatt, T. Zanon-Willette, S. M. Foreman, and J. Ye, Nuclear spin effects in optical lattice clocks, Phys. Rev. A **76**, 022510 (2007).

[48] L. Olschewski, Determination of the nuclear magnetic moments on free ^{43}Ca-, ^{87}Sr-, ^{135}Ba-, ^{137}Ba-, ^{171}Yb- and ^{173}Yb-atoms by means of optical pumping, Z. Phys. **249**, 205 (1972).
[49] F. D. Feiock and W. R. Johnson, Relativistic evaluation of internal diamagnetic fields for atoms and ions, Phys. Rev. Lett. **21**, 785 (1968).
[50] G. H. Fuller, Nuclear spins and moments, J. Phys. Chem. Ref. Data **5**, 835 (1976).
[51] V. A. Dzuba and A. Derevianko, Dynamic polarizabilities and related properties of clock states of the ytterbium atom, J. Phys. B **43**, 074011 (2010).
[52] K. Beloy, W. F. McGrew, X. Zhang, D. Nicolodi, R. J. Fasano, Y. S. Hassan, R. C. Brown, and A. D. Ludlow, Modeling motional energy spectra and lattice light shifts in optical lattice clocks, Phys. Rev. A **101**, 053416 (2020).
[53] S. Blatt, J. W. Thomsen, G. K. Campbell, A. D. Ludlow, M. D. Swallows, M. J. Martin, M. M. Boyd, and J. Ye, Rabi spectroscopy and excitation inhomogeneity in a one-dimensional optical lattice clock, Phys. Rev. A **80**, 052703 (2009).
[54] H. Kim, M.-S. Heo, C. Y. Park, D.-H. Yu, and W.-K. Lee, Absolute frequency measurement of the ^{171}Yb optical lattice clock at KRISS using TAI for over a year, Metrologia **58**, 055007 (2021).
[55] V. D. Ovsiannikov, V. G. Pal'Chikov, A. V. Taichenachev, V. I. Yudin, and H. Katori, Multipole, nonlinear, and anharmonic uncertainties of clocks of Sr atoms in an optical lattice, Phys. Rev. A **88**, 013405 (2013).
[56] K. Beloy (to be published).
[57] T. Kobayashi, D. Akamatsu, Y. Hisai, T. Tanabe, H. Inaba, T. Suzuyama, F.-L. Hong, K. Hosaka, and M. Yasuda, Uncertainty evaluation of an ^{171}Yb optical lattice clock at NMIJ, IEEE Trans. Ultrason. Ferroelectr. Freq. Control **65**, 2449 (2018).
[58] M. Pizzocaro, F. Bregolin, P. Barbieri, B. Rauf, F. Levi, and D. Calonico, Absolute frequency measurement of the $^1S_0 - {}^3P_0$ transition of ^{171}Yb with a link to international atomic time, Metrologia **57**, 035007 (2020).
[59] S. G. Porsev, M. S. Safronova, U. I. Safronova, and M. G. Kozlov, Multipolar polarizabilities and hyperpolarizabilities in the Sr optical lattice clock, Phys. Rev. Lett. **120**, 063204 (2018).
[60] F.-F. Wu, Y.-B. Tang, T.-Y. Shi, and L.-Y. Tang, Dynamic multipolar polarizabilities and hyperpolarizabilities of the Sr lattice clock, Phys. Rev. A **100**, 042514 (2019).
[61] V. D. Ovsiannikov, S. I. Marmo, S. N. Mokhnenko, and V. G. Palchikov, Higher-order effects on uncertainties of clocks of Mg atoms in an optical lattice, J. Phys. Conf. Ser. **793**, 012020 (2017).
[62] F.-F. Wu, Y.-B. Tang, T.-Y. Shi, and L.-Y. Tang, Magic-intensity trapping of the Mg lattice clock with light shift suppressed below 10^{-19}, Phys. Rev. A **101**, 053414 (2020).
[63] S. G. Porsev and M. S. Safronova, Calculation of higher-order corrections to the light shift of the $5s^2\ {}^1S_0 - 5s5p\ {}^3P_0^o$ clock transition in Cd, Phys. Rev. A **102**, 012811 (2020).
[64] L. Wu, X. Wang, T. Wang, J. Jiang, and C. Dong, Be optical lattice clocks with the fractional Stark shift up to the level of 10^{-19}, New J. Phys. **25**, 043011 (2023).
[65] R. Szmytkowski, Larmor diamagnetism and Van Vleck paramagnetism in relativistic quantum theory: The Gordon decomposition approach, Phys. Rev. A **65**, 032112 (2002).
[66] W. Kutzelnigg, Diamagnetism in relativistic theory, Phys. Rev. A **67**, 032109 (2003).
[67] N. Shiga, W. M. Itano, and J. J. Bollinger, Diamagnetic correction to the ^{9}Be$^+$ ground-state hyperfine constant, Phys. Rev. A **84**, 012510 (2011).
[68] The quadratic Zeeman shift coefficient for the clock transition is reported as −0.060 95(7) Hz/G^2 in Ref. [2]. Here, we report a corrected value of −0.059 97(7) Hz/G^2, as discussed in the Supplemental Material [32].

End Matter

Appendix: Born-Oppenheimer + WKB *approximation*—The lattice light shift model in the main text follows a standard harmonic basis treatment [18]. While it gives important physical intuition, these models are known to break down at higher temperatures as they fail to capture axial-radial couplings [52]. Considering our radial temperature of ∼600 nK (∼1 μK in the running wave measurements), we elect to perform an additional analysis using a Born-Oppenheimer + WKB treatment (BO+ WKB) which better captures axial-radial couplings [52]. In this treatment the lattice light shift is given by

$$\frac{\delta\nu_{LS}(u,\delta_L,n_z,T_r)}{\nu_c} \approx -\sum_{n_z} W_{n_z}\left[\frac{\partial\tilde{\alpha}_{E1}}{\partial\nu}\delta_L X(n_z,u_0,T_r)u_0 + \tilde{\alpha}_{M1E2}Y(n_z,u_0,T_r)u_0 + \tilde{\beta}Z(n_z,u_0,T_r)u_0^2\right], \tag{A1}$$

where W_{n_z} is an n_z band weight and u_0 is the peak trap depth normalized by E_R. $X(n_z,u_0,T_r)$, $Y(n_z,u_0,T_r)$, and $Z(n_z,u_0,T_r)$ are trap depth reduction factors which are numerically calculated [52]. As presented in Table III, we find good agreement between models, but note a 1-σ discrepancy of $(\partial\tilde{\alpha}_{E1}/\partial\nu)$. We note that future evaluations with improved uncertainties will likely need to utilize colder temperatures to continue to employ the harmonic basis model.

TABLE III. Comparison of experimental results as derived from either the harmonic [Eq. (1)] or BO + WKB [Eq. (1)] treatment.

Coefficient	Harmonic basis	BO + WKB
$(\partial\tilde{\alpha}_{E1}/\partial\nu)$ $(10^{-20}/\mathrm{MHz})$	4.21(10)	4.31(9)
$\tilde{\beta}$ (10^{-21})	−1.7(4)	−2.0(6)
$\tilde{\alpha}_{M1E2}^{\mathrm{Experiment}}$ (10^{-18})	−1.41(9)	−1.45(8)
ν_{E1} (MHz)	394 798 266.9(26)	394 798 266.3(30)
$\nu_r'(0)$ (MHz)	394 798 300.4(18)	394 798 300.0(25)